The Astrophysical Journal, 825:32 (9pp), 2016 July 1 doi:10.3847/0004-637X/825/1/32

FAR INFRARED VARIABILITY OF SAGITTARIUS A*: 25.5 hr OF MONITORING WITH *HERSCHEL**

Jordan M. Stone[1], D. P. Marrone[1], C. D. Dowell[2], B. Schulz[3], C. O. Heinke[4,5,7], and F. Yusef-Zadeh[6]

[1] Steward Observatory, University of Arizona, 933 N. Cherry Ave, Tucson, AZ 85721-0065, USA; jstone@as.arizona.edu, dmarrone@as.arizona.edu

[2] Jet Propulsion Laboratory, 4800 Oak Grove Drive, Pasadena, CA 91109, USA; charles.d.dowell@jpl.nasa.gov

[3] Infrared Processing and Analysis Center, MS 100-22, California Institute of Technology, JPL, Pasadena, CA 91125, USA; bschulz@ipac.caltech.edu

[4] Dept. of Physics, CCIS 4-183, University of Alberta, Edmonton, AB T6G 2E1, Canada; heinke@ualberta.ca

[5] Max Planck Institut für Radioastronomie, Auf dem Hügel 69, D-53121 Bonn, Germany

[6] Department of Physics and Astronomy and CIERA, Northwestern University, Evanston, IL 60208, USA; zadeh@northwestern.edu

Received 2015 August 18; revised 2016 May 2; accepted 2016 May 13; published 2016 June 27

ABSTRACT

Variable emission from Sgr A*, the luminous counterpart to the super-massive black hole at the center of our Galaxy, arises from the innermost portions of the accretion flow. Better characterization of the variability is important for constraining models of the low-luminosity accretion mode powering Sgr A*, and could further our ability to use variable emission as a probe of the strong gravitational potential in the vicinity of the $4 \times 10^6 M_\odot$ black hole. We use the *Herschel* Spectral and Photometric Imaging Receiver (SPIRE) to monitor Sgr A* at wavelengths that are difficult or impossible to observe from the ground. We find highly significant variations at 0.25, 0.35, and 0.5 mm, with temporal structure that is highly correlated across these wavelengths. While the variations correspond to $<1\%$ changes in the total intensity in the *Herschel* beam containing Sgr A*, comparison to independent, simultaneous observations at 0.85 mm strongly supports the reality of the variations. The lowest point in the light curves, ~0.5 Jy below the time-averaged flux density, places a lower bound on the emission of Sgr A* at 0.25 mm, the first such constraint on the THz portion of the spectral energy distribution. The variability on few hour timescales in the SPIRE light curves is similar to that seen in historical 1.3 mm data, where the longest time series is available, but the distribution of variations in the sub-mm do not show a tail of large-amplitude variations seen at 1.3 mm. Simultaneous X-ray photometry from *XMM-Newton* shows no significant variation within our observing period, which may explain the lack of very large submillimeter variations in our data if X-ray and submillimeter flares are correlated.

Key words: accretion, accretion disks – black hole physics – Galaxy: center

1. INTRODUCTION

Sagittarius A* (Sgr A*) is the luminous source ($L \sim 10^{-8} L_{\rm Edd}$; Genzel et al. 2010) associated with the super-massive black hole at the center of our Galaxy ($M = 4 \times 10^6 M_\odot$, $D = 8.3$ kpc; Ghez et al. 2008; Gillessen et al. 2009). Due to its mass, relative proximity, and faintness, Sgr A* is the premier target for studies of strong gravity, low-luminosity accretion flows, and quiescent galactic nuclei.

Variable emission from Sgr A* arises from deep in the potential well of the black hole in the innermost regions of the accretion flow (Baganoff et al. 2001; Genzel et al. 2003; Doeleman et al. 2008; Fish et al. 2011; Dexter et al. 2014). Thus, features in the light curve of Sgr A* could provide a powerful probe of both the physics of the flow and the gravitational potential around the black hole, yet the nature of the variability is not fully understood.

Constraining the radiative mechanisms responsible for the luminosity of Sgr A* is complicated by the difficulties associated with measuring the spectral energy distribution (SED). At many wavelengths, Sgr A* is either obscured by the galaxy or confused with gas (radio and X-ray), dust (submillimeter), or stars (near-infrared), and intrinsic variability imposes a need for simultaneous observations in as many bands as possible. Many groups have coordinated multi-facility observing campaigns to constrain the shape of the quiescent, or time-averaged, SED and the spectral shape of variable emission (e.g., Falcke et al. 1998; Eckart et al. 2004, 2008; An et al. 2005; Yusef-Zadeh et al. 2006; Marrone et al. 2008; Dodds-Eden et al. 2009; Haubois et al. 2012; Brinkerink et al. 2015). The quiescent SED rises from centimeter to millimeter wavelengths, peaks around 0.8 mm (in flux density units; (Marrone et al. 2006; Bower et al. 2015), and declines through the IR and X-ray—the only other wavelengths where Sgr A* has been clearly detected. The $S_\nu \sim \lambda^{-0.5}$ radio spectrum is consistent with optically thick, stratified synchrotron emission (de Bruyn 1976), and the increasing slope ($S_\nu \sim \lambda^{-1}$) near the spectral peak, the "submillimeter bump" (Falcke et al. 1998), has been interpreted as coming from the innermost regions of the accretion flow (Falcke et al. 1998; Doeleman et al. 2008; Dexter et al. 2010). The transition from optically thick to thin emission appears to occur over a range of wavelengths in the millimeter/submillimeter regime (Marrone et al. 2006; Bower et al. 2015).

Studies of the variability of Sgr A* have revealed some patterns in the changes between wavelengths. X-ray and IR monitoring has shown that X-ray flares are accompanied by IR flares whenever there is simultaneous IR data (Hornstein et al. 2007) but that IR flares are not always accompanied by X-ray flares. The relationship between millimeter/submillimeter light curves and features in NIR/X-ray light curves is less well understood. Some report evidence for increased emission in the millimeter/submillimeter after spikes in the NIR/X-ray (Yusef-Zadeh et al. 2006; Eckart et al. 2008; Marrone et al. 2008). These authors argue that the delay is due to the adiabatic expansion of a synchrotron-emitting plasma,

* *Herschel* is an ESA space observatory with science instruments provided by European-led Principal Investigator consortia and with important participation from NASA.

[7] Humboldt Fellow.

whose peak emission shifts toward longer wavelengths as the expanding blob cools and becomes less dense. Models including multiple expanding synchrotron-emitting blobs have been tuned to provide adequate fits to simultaneous submillimeter, NIR, and X-ray flares (Eckart et al. 2006, 2009, 2012; Yusef-Zadeh et al. 2006, 2008, 2009). These models often predict that the spectrum of observed flares should peak at wavelengths $\lesssim$0.3 mm, impossible to constrain from the ground. The expanding blob scenario is consistent with the results of Hornstein et al. (2007), who did not observe a change in the NIR spectral slope during a flare. The absence of a change in spectral slope can be explained with a non-radiative cooling mechanism, such as adiabatic expansion (Marrone et al. 2008). However, other groups do report NIR spectral slope changes during flux increases (e.g., Gillessen et al. 2006).

Other authors suggest that millimeter/submillimeter light curves are anti-correlated with NIR/X-ray features (Yusef-Zadeh et al. 2010; Haubois et al. 2012). This could be due to reduced millimeter/submillimeter emissivity caused by a reduction of the magnetic field strength or a loss of electrons due to acceleration or escape—all of which are expected outcomes of a magnetic reconnection event (Dodds-Eden et al. 2010; Haubois et al. 2012). Alternatively, the reduced millimeter/submillimeter flux density coincident with NIR/X-ray features could be due to obscuration of the quiescent emission region by the excited NIR/X-ray emission region (Yusef-Zadeh et al. 2010). Dexter & Fragile (2013) model time-dependent emission from Sgr A* and show that NIR/X-ray features and submillimeter features arise from different electrons so are not necessarily related, yet they demonstrate how cross-correlation analysis can produce spurious peaks. Thus, not all reported correlations between IR and millimeter/submillimeter wavelengths may be evidence for a physical connection.

Another challenge for ground-based studies of Sgr A* variability is adequately sampling the relevant timescales. In the NIR, a break in the power spectrum of variations has been reported on timescales ~3 hr (Meyer et al. 2009), while at millimeter/submillimeter wavelengths there appears to be a characteristic timescale for variations similar to the ~6 hr observing windows available to northern hemisphere submillimeter telescopes. Space-based observatories can observe Sgr A* for longer intervals and can provide more accurate and precise probes of these important timescales (e.g., Hora et al. 2014).

Relatively little is known about Sgr A* at the wavelengths probed by the *Herschel* Spectral and Photometric Imaging Receiver (SPIRE, Griffin et al. 2010). SPIRE observes in three bands simultaneously: 0.5, 0.35, and 0.25 mm. A few ground-based observations at 0.45 and 0.35 mm have been made when excellent weather provided adequate atmospheric transparency. At 0.45 mm, single dish measurements have detected Sgr A* at ~1.2 Jy and at ~4 Jy, although ~1 Jy uncertainty in the absolute flux density is incurred due to confusion with extended dust emission (e.g., Pierce-Price et al. 2000; Marrone et al. 2008; Yusef-Zadeh et al. 2009). Marrone et al. (2006) made interferometric measurements at 0.43 mm that resolved Sgr A* from surrounding emission. Those measurements revealed a flat 1.3–0.43 mm spectral slope and detected variability of ~3 Jy. At 0.35 mm, atmospheric opacity and confusion with dust are even more severe, yet a small number of measurements have been made from the ground that suggest variability by a factor ~3 (Serabyn et al. 1997; Marrone et al. 2008; Yusef-Zadeh et al. 2009).

Both theoretical predictions from model-fits to multi-wavelength flare data (Eckart et al. 2006, 2009), and observational hints from sparse inhomogeneous ground-based observations suggest that the variability of Sgr A* in the SPIRE bands may be stronger than the variability seen at ~1.3 mm (the typical variability amplitude at 1.3 mm is ~1 Jy on long timescales Dexter et al. 2014). SPIRE provides a unique opportunity to test the model predictions and to compile a uniform and sensitive dataset at 0.5, 0.35, and 0.25 mm. In this paper we use 25.5 hr of *Herschel* SPIRE data, together with overlapping X-ray and 0.85 mm observations provided by *XMM-Newton* and the CSO to monitor for variability and constrain the spectral shape of flares.

Table 1
Herschel SPIRE ObsIDs

First Interval	Second Interval
1342227655	1342227733
1342227656	1342227734
1342227657	1342227735
1342227658	1342227736

Note. Observations were split into two intervals separated by 1 day. We reduced each interval individually due to the large computer memory demands of the calibration algorithms included in HIPE

2. OBSERVATIONS AND REDUCTION

The data we present in this paper were collected as part of a multi-facility observing campaign to monitor Sgr A*. The participating observatories included *Herschel*, CSO, *XMM-Newton*, and the SMA.

2.1. Herschel SPIRE

SPIRE data were collected in two 12.75 hr blocks: the first from 2011 August 31 22:04 UT through 2011 September 01 10:51 UT; and the second from 2011 September 01 20:33 through 2011 September 02 9:20. Each interval includes 668 scans across the Galactic Center. Table 1 shows the observation identifiers (ObsIDs) downloaded from the *Herschel* Science Archive for this work.

We reprocessed the SPIRE data products using the *Herschel* HIPE software to include the extended flux density gain calibration data products in version 3.1 of the HIPE calibration tree. This step normalizes the response of each bolometer integrated over the beam area, rather than to the peak flux density, which is more appropriate for fields with extended emission. We also chose to include the scan turnarounds in our reprocessing and map making. This option provides additional points on the sky where bolometers make overlapping measurements, increasing the constraints on the calibration algorithms.

For each interval, we concatenated all the Level 1 scans from each SPIRE array for each ObsID array into a single Level 1 context to feed to the HIPE destriper[8] (Schulz, B., et al. 2016, in preparation). The destriper iteratively determines offsets for all scans crossing the mapped region on the sky. Each scan

[8] We used the destriper included with the unreleased development version of HIPE 14.0.2035, which provided improved convergence.

consists of many detector readouts. The iterations stop when the variances of the readouts within the boundaries of the map pixels cannot be further improved. By running the destriper in "perScan"-mode, individual offsets—we used a 0° polynomial—are fitted for each scan of a given detector, compensating for any long-term variations in the scans. We ran the destriper twice, using the output diagnostic table and destriped scans as inputs for the destriper on the second iteration. This provided small improvements.

Although our relative detector calibration is optimized for extended sources, we produced maps calibrated in units of Jy beam^{-1}. To do this, we binned the scans into groups of 4, and made a single map for each bin, resulting in a time resolution of 4.6 minute per map. We assigned the same sky coordinates to each pixel in each map, taking care to center the location of Sgr A* in the central pixel.

Preliminary review of the maps revealed motion of the flux density distribution with respect to the pixels. This motion is due to insufficiently reconstructed pointing drifts of the telescope that result in inaccurate sky coordinates associated with each bolometer readout. Uncorrected, these drifts limit the precision with which we can calibrate the bolometers and extract light curves.

We solved for pointing offsets as a function of time by shifting each map to best align with the first map produced for each observing interval. Total drifts over the 12.75 hr observing intervals were $\sim 2''$ and $\sim 1''$ for the observations starting 2011 August 31 and 2011 September 01, respectively. This is consistent with pointing uncertainties given by Sánchez-Portal et al. (2014).

After solving for the best-fit shifts, we updated the coordinates of the SPIRE scans in HIPE and re-ran the destriper and our mapping routine. We iterated the whole process once, and the results showed that our shifts had converged. A small residual drift, $\sim 0.''2$, remains in the data.

Due to the bright extended emission of the Sgr A complex at the Galactic Center, and because of the relatively large beam size delivered by *Herschel* ($18''$, $25''$, and $36''$ at 0.25 mm, 0.35 mm, and 0.5 mm, respectively) Sgr A* is not separated from its surroundings. However, Sgr A* is expected to be the only intrinsically variable source in our maps (there is a magnetar, SGR J1745-2900, that is about $2.''4$ away from Sgr A*, but the magnetar was in its quiescent phase when these X-ray/submillimeter observations were carried out; Kennea et al. 2013). Therefore, we extract variability light curves from difference images, subtracting the mean map of each 12.75 hr observation from the 4 minute sub-maps.

We performed photometry on the difference maps by scaling a 1 Jy beam^{-1} reference point-spread function to best fit our observations. We downloaded the reference beams for each waveband from the SPIRE public wiki.[9] Specifically, we combined our observed difference maps (D_{ij}), a variance map created by calculating the variance of all bolometer readouts contributing to a given map pixel (σ_{ij}^2), and the PSF (P_{ij}) as follows:

$$\bar{f} = \frac{\sum_{ij}\left(\frac{P_{ij}^2}{\sigma_{ij}^2}\right) f_{ij}}{\sum_{ij}\left(\frac{P_{ij}^2}{\sigma_{ij}^2}\right)}, \quad (1)$$

which is the inverse variance weighted mean of the scale factor

$$f_{ij} = \frac{D_{ij}}{P_{ij}}. \quad (2)$$

The variance of our measured scale factor can then be computed using

$$\bar{\sigma}^2 = \frac{\sum_{ij}\left(\frac{P_{ij}^2}{\sigma_{ij}^2}\right)(f_{ij} - \bar{f})^2}{\sum_{ij}\left(\frac{P_{ij}^2}{\sigma_{ij}^2}\right)}. \quad (3)$$

We extracted light curves from the location of Sgr A* and several reference locations. Reference light curves should show no intrinsic variability so serve as indicators of time variable systematic problems. We chose reference locations as follows: First, we generated 100 random locations within 2 arcmin of Sgr A*. From that set we excluded any points whose average flux density was not within a factor of two of the average flux density at the position of Sgr A*. We also excluded points where the local spatial gradient had a magnitude that was not within a factor of two of the gradient at the location of Sgr A*. We then searched the remaining locations for a maximal set with no two references within $40''$. This last criterion ensures that the 0.5 mm beam does not overlap at the 50% level for any of our reference locations. Using this approach we identified 12 locations on the map for use as references.

We noticed that many of our reference light curves were affected by a small linear trend across the observing interval. This trend was largest in the 0.25 mm band where the average slope was measured to be ~ -0.02 Jy h^{-1}. The steepest slope removed from our reference light curves was ~ -0.1 Jy h^{-1}. These values are consistent with the trends expected given the residual pointing drift that remains in the maps and the flux density gradients at the locations of our references. Since these drifts strongly affect the appearance of the inter-band cross-correlations (resulting in relatively high power over a large range of lags) we subtract a best-fit line from each light curve. Unfortunately, this correction precludes a meaningful test of whether our light curves are stationary (a time series is stationary if there are no changes in its mean value or variance and there are no periodic components, Chatfield 1989). However, in Section 4 we quantify changes in the variance of our light curves in subintervals of four-hour length.

Our calculated errorbars (Equation (3)) were over estimated for each location, including Sgr A*. This was obvious given the magnitude of the point to point variations in the light curves and the much larger size of the calculated errorbars. The over-sized errorbars result from the way that our variance maps are produced. In HIPE, variance maps are produced by binning all bolometer readouts that occur within a given pixel without respect to where within a pixel a readout occurs. In regions of complex structure, such as Sgr A, spatial flux density gradients will lead to variations in flux density values within a pixel, inflating the variance. To account for this, we scaled the errorbars for each reference light curve to provide a good fit to a constant zero-flux model (reduced $\chi^2 = 1$). Typical scale factors were ~ 0.3. We took the mean scale factor and applied it to the errorbars for the light curve of Sgr A*. This approach provides empirically accurate errorbars that maintain appropriate relative size as a function of time and location on the map.

[9] https://nhscsci.ipac.caltech.edu/sc/index.php/Spire/PhotBeamProfileDataAndAnalysis

2.2. Caltech Submillimeter Observatory 0.85 mm

Ground-based observations with the SHARC II camera at the CSO provided 0.85 mm monitoring from 2011 September 1 04:25 UT through 09:04 UT, and from 2011 September 2 03:35 UT through 09:00 UT, overlapping each of our *Herschel* observing intervals. A 3′ field surrounding Sgr A* was observed with Lissajous scanning of the telescope with an amplitude of 100″ and a period of 20 s (Yusef-Zadeh et al. 2006, 2008). On both evenings, the conditions were suitable for observation for the full periods, with clear skies or light cirrus, low wind, and moderate humidity. The zenith atmospheric opacity at 225 GHz was ∼0.14 on September 1 and ∼0.10 on September 2. The telescope focus was monitored and, as needed, adjusted during separate observations of point sources, accounting for the gaps in the light curves; the larger gap around 6:00 UT on September 2 was due to a brief observation of Sgr A* at 0.35 mm which did not yield useful results.

Data analysis, including absolute calibration, followed the method described by Yusef-Zadeh et al. (2009). Sgr A* is not well resolved from surrounding dust emission with the 19″ resolution of CSO at 0.85 mm. This adds ∼1 Jy uncertainty to the absolute flux level of Sgr A* measured at 0.85 mm, but the measurement of variations is much more precise. Uncertainties for each 0.85 mm measurement were derived from the rms in the image, from which the mean image and a Gaussian at the position of Sgr A* have been subtracted.

2.3. XMM-Newton

XMM-Newton data were collected in two blocks, the first (ObsID 0658600101) from 2011 August 31 at 23:37 UT to September 1 at 12:58 UT, and the second (ObsID 0658600201) from 2011 September 1 at 20:26 to September 2 at 10:42 UT. Sgr A* was placed at the center of the *XMM-Newton*/EPIC field of view (away from any chip gaps). The medium filter, and full-frame mode, were used for all three EPIC instruments. The more sensitive pn camera (Strüder et al. 2001) had exposures of 41.9 and 45.2 ks in the two observations, respectively. The less sensitive MOS1 and MOS2 cameras (Turner et al. 2001) had exposures of 48.6 and 52.3 ks in the two observations. Below we focus on results from the pn camera; the MOS results were similar.

The data were processed with the *XMM* Science Analysis Software (version 11.0.0) to select PATTERN $\leqslant$ 12, energies between 2 and 10 keV, and FLAG = 0. We extracted light curves at 300 s binning from a radius of 10 arcsec (as typical for Sgr A*, e.g., Porquet et al. 2003), centered at the location of Sgr A*. This radius only encloses 50% of the emission from Sgr A* (Read et al. 2011), yet includes a significant amount of contamination from unrelated sources, both diffuse and point-like. In fact, the quiescent flux of Sgr A* (2–10 keV $L_X \sim 2.4 \times 10^{33}$ erg s^{-1}) is only ∼10% of the flux enclosed within 10″ (Baganoff et al. 2003).

No statistically significant (3σ) flares were observed in any of the EPIC light curves, and the highest points in each lightcurve did not correspond with the highest points in other light curves. The most interesting possible peak occurred at 4.85 hr into the first observation, reaching 0.153 ± 0.023 counts s^{-1}, compared to an average rate of 0.10 counts s^{-1}. We can thus set an upper limit on the background subtracted Sgr A* flare luminosity during our observations (for flares of 300 s in length) of 7.6 times the quiescent value, or L_X (2–10 keV) $< 1.8 \times 10^{34}$ erg s^{-1}; longer flares have stricter upper limits ($<6 \times 10^{33}$ erg s^{-1} on average for 1 ks flares). We assume an absorbed power-law spectrum for the X-ray flares, as seen for the quiescent Sgr A* spectrum (Baganoff et al. 2003), with photon index of 2.7 and $N_H = 9.8 \times 10^{22}$ cm^{-2}. Fits to the spectra of X-ray flares from Sgr A* span a range of spectral indices, from 1.7 to 3.2; changing the assumed spectral index in this range of photon indices alters the upper limits by 10% up or down.

2.4. SMA 1.3 mm

In an attempt to provide overlapping 1.3 mm data, Sgr A* was also observed with the SMA. Unfortunately, it was afternoon in Hawaii during our *Herschel* and *XMM-Newton* observations. SMA observing conditions are typically worst in the afternoon because the unstable atmosphere corrupts the interferometer phases. Given the poor quality of the data we can only put a ∼30% upper limit on the amplitude of variations of Sgr A* during our observations. This corresponds to ∼1 Jy, which is about the size of the largest variations seen at 1.3 mm (Dexter et al. 2014).

3. RESULTS

We show our average SPIRE maps of the Galactic Center in Figure 1. On each map, we overlay contours of the *Herschel* beam at the location of Sgr A*. While the beam size at 0.25 mm is smaller than at the longer wavelengths, the dust emission at this wavelength is significantly stronger. The net result is a more challenging measurement at 0.25 mm. For an analysis of the dust properties at the Galactic Center, using SPIRE maps as well as additional far-infrared data, see Etxaluze et al. (2011).

We show our Sgr A* X-ray and submillimeter light curves for both observation intervals in Figures 2 and 3. There are significant variations in all of the SPIRE bands. Ground-based 0.85 mm data closely track the SPIRE bands during the first interval. The most significant feature, a flux density decrement, occurs just before 05:00 UT on September 1st, and is captured by both *Herschel* and the CSO. The magnitude of the dip, ∼0.5 Jy, was similar in all bands, and for the *Herschel* bands corresponds to 0.6%, 0.8%, and 0.5% of the flux density in the beam containing Sgr A*. The dip coincides with a marginal feature in the X-ray light curve, which we highlight with a vertical dashed line. This behavior is reminiscent of the data reported in other studies that show ∼0.6 to 1 Jy decrements in millimeter light-curves correlated with flares in the near-infrared and X-ray (Dodds-Eden et al. 2010; Yusef-Zadeh et al. 2010; Haubois et al. 2012).

The significance of features seen in the SPIRE light curves is supported by cross-correlation. In Figure 4 we show the cross-correlation of the light curves for each pair of SPIRE bands, for each observing interval. We show cross-correlations for Sgr A* (black curves), and each of the 12 reference locations (gray curves).

All pairs of Sgr A* light curves are more correlated than pairs from the reference locations. This implies the presence of a shared signal, stronger than the residual systematics that could result in spurious zero-lag correlations for the references (e.g., pointing inaccuracies and thermal drifts). The absence of dominant systematics in these ∼0.5% difference measurements is also indicated by the agreement with the independent measurements made by the CSO. Cross-correlation peaks for

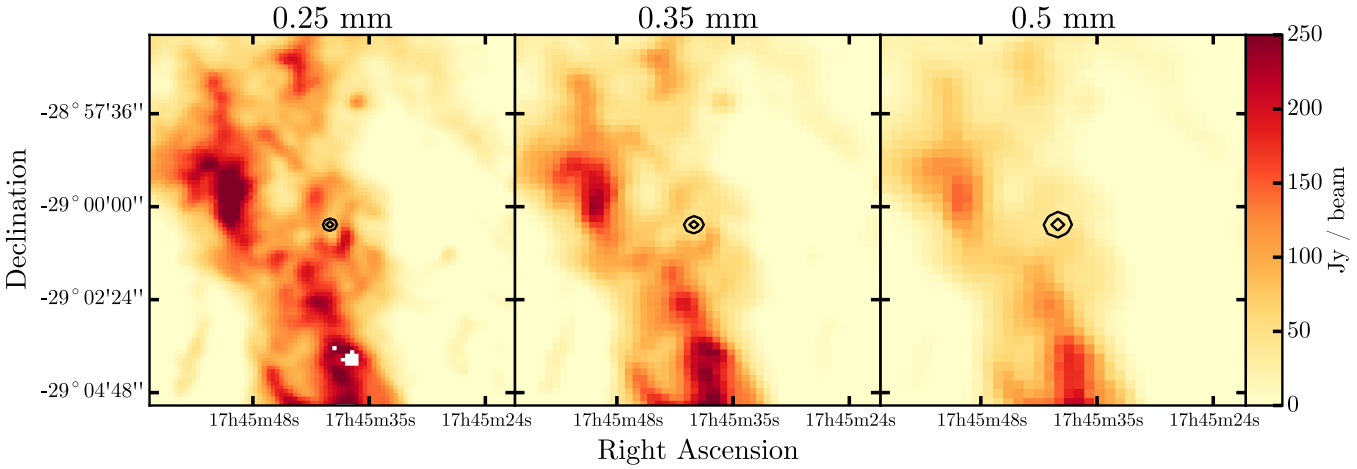

Figure 1. *Herschel* SPIRE maps of the galactic center. From left to right are the maps at 0.25 mm, 0.35 mm, and 0.5 mm, respectively. Each map is $11' \times 10'$. On each, we show the 80% and 50% contours of the *Herschel* beam centered at the location of Sgr A*. Sgr A* is not resolved from its surroundings. For some map pixels the strong extended emission from the Galactic Center region exceeded the dynamic range of the SPIRE readout electronics in our chosen instrument setup, which was an accepted trade-off to achieve a maximum sensitivity. This leads to some holes in the 0.25 mm map (white pixels).

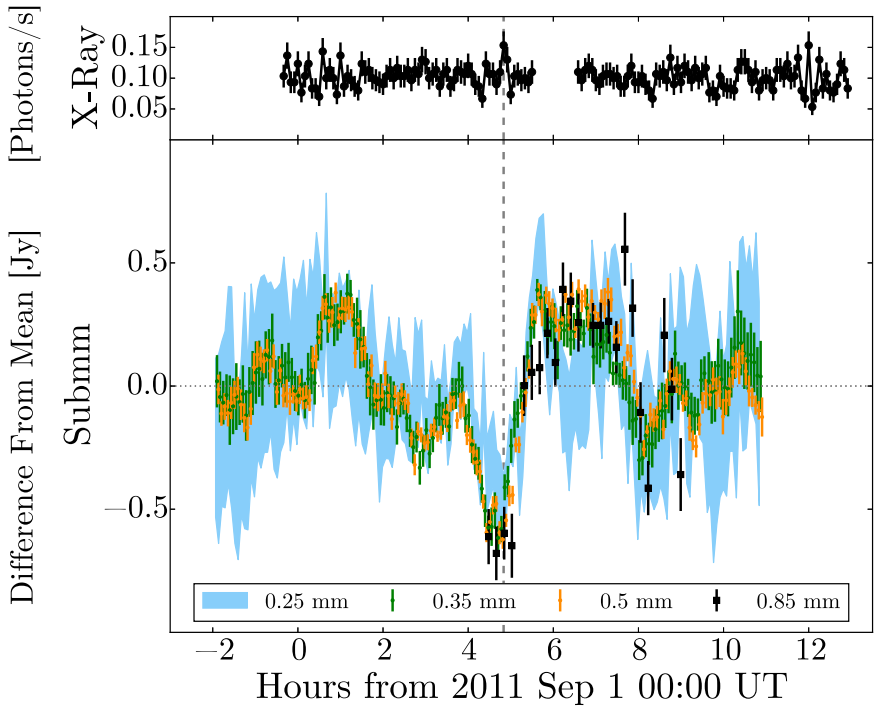

Figure 2. Light curves from our first observing interval. Upper panel: *XMM-Newton* pn camera X-ray light curve. Lower panel: SPIRE and CSO submillimeter light curves. For clarity in presenting four overlapping light curves, we have employed two different plotting methods. The 0.25 mm light curve is shown with a light-blue swath that indicates the 1-σ confidence region. The 0.35, 0.5, and 0.85 mm light curves are displayed with dots and errorbars indicating 1-σ confidence. The SPIRE bands have each been offset slightly in time to avoid overlap.

curves including the 0.25 mm light curve from our first observing interval occur lagged by 4 minute, or one sample. All the other cross-correlation curves show zero lag.

4. DISCUSSION

4.1. Variability Amplitude Compared to 1.3 mm

We observe strong variations in all three SPIRE bands with similar amplitude in each. We do not know the absolute flux density of Sgr A* at any of these wavelengths due to confusion with the surrounding dust emission (though interferometer measurements at 0.43 mm in Marrone et al. (2006) show a minimum flux density of 2 Jy in 4 epochs). However, the negative deviation around 5 UT in the first interval implies that for all three bands there must be a minimum time-averaged flux density of at least 0.5 Jy, even at 0.25 mm where the SED is not otherwise constrained.

We now attempt to provide an empirical comparison of Sgr A* variability at SPIRE wavelengths to variability at 1.3 mm. Dexter et al. (2014) provide a detailed analysis of Sgr A* variability at 1.3, 0.8, and 0.43 mm. They demonstrated consistent variability amplitude characteristics between the bands, though the 0.8 mm and especially the 0.43 mm characteristics were poorly constrained due to the smaller number of measurements at those

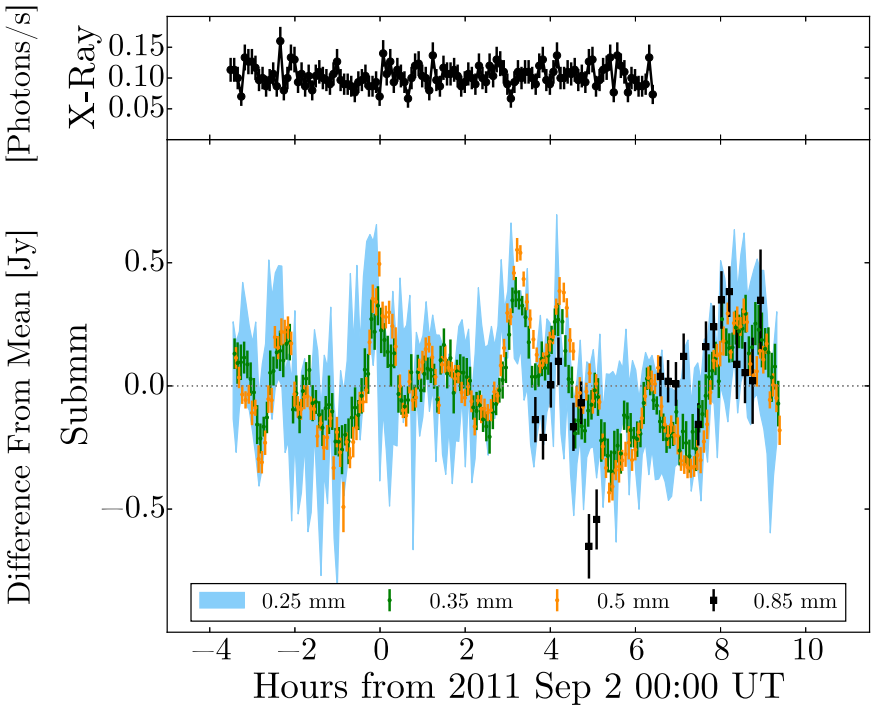

Figure 3. Same as Figure 2 but for our second observing interval.

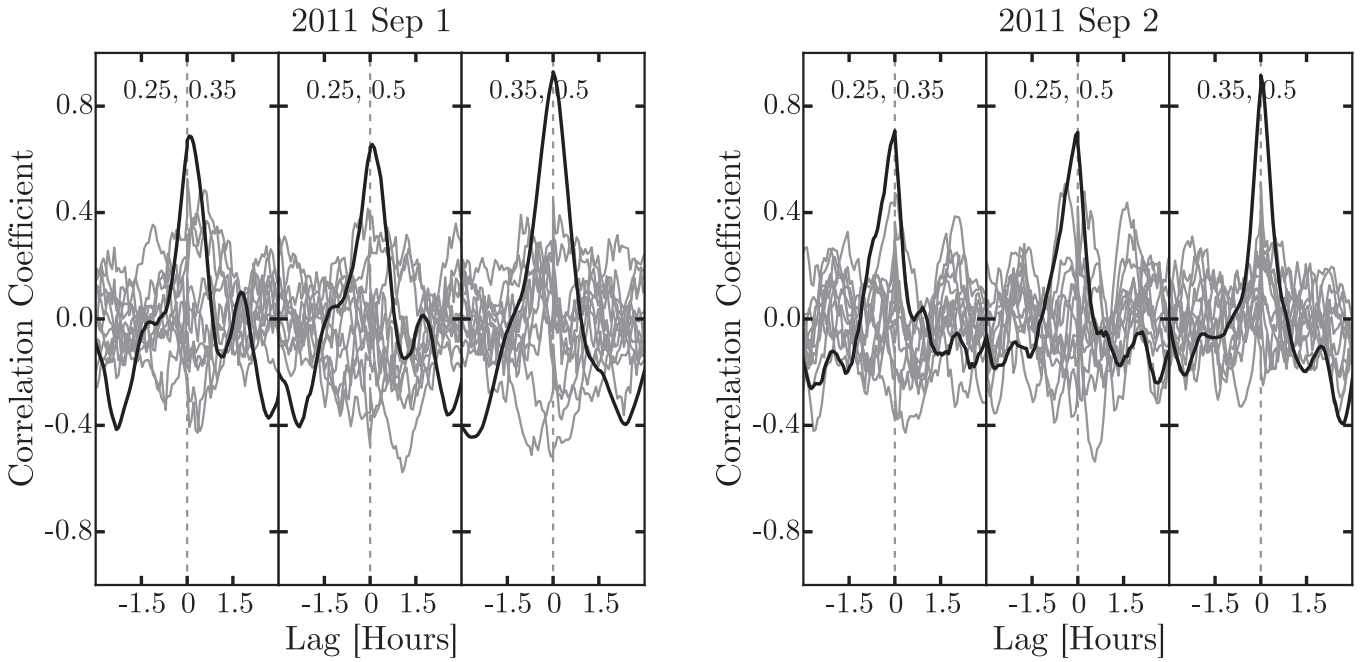

Figure 4. Cross correlations for all three pairs of SPIRE bands for Sgr A* (black line) and reference locations (gray lines). Left: data from the first observing interval. Right: data from the second observing interval. In each panel, the left column shows the cross-correlation of the 0.25 mm light curve with the 0.35 mm light curve, the middle column shows the cross-correlation of the 0.25 mm light curve with the 0.5 mm light curve, and the right column shows the cross-correlation of the 0.35 mm light curve and the 0.5 mm light curve.

wavelengths. To compare our light curves to 1.3 mm observations composed of many shorter intervals of irregularly sampled data, we devised the approach described below.

Using the SPIRE light curves, as well as the ∼70 hr of 1.3 mm light curves compiled by Dexter et al. (2014), we determine most-likely variability amplitudes for overlapping 4 hr subsets of the data at each wavelength and compile them into a distribution function. The segmentation time is chosen to span typical variations in the light curves, though our results are not very sensitive to the choice. We used overlapping segments, whose start times were separated by at least 1.33 hr (66% overlap), to provide additional measurements of σ. Explicitly, for each four-hour block, we binned the data to 20 minute time resolution for better signal-to-noise, subtracted

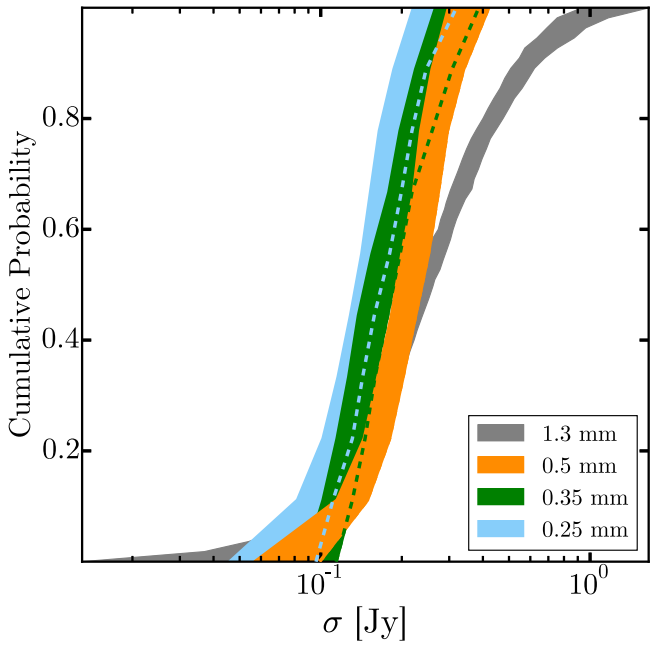

Figure 5. Cumulative distribution of variability amplitude in overlapping 4 hr blocks. The width of each swath contains the central 68% of CDFs for each light curve, generated by sampling the likelihood function of σ for each 4 hr block. (See text for details.) Where obscured, dashed lines indicate the edge of each swath.

the bin mean, and then constructed the function

$$P_{\rm block}(\sigma|f_i,\,\delta_i) = \Pi_i\left(\frac{1}{\sqrt{2\pi}\,(\sigma^2+\delta_i^2)}\right)e^{\left(\frac{-f_i^2}{2(\sigma^2+\delta_i^2)}\right)}, \qquad (4)$$

for the probability that σ is the typical variability amplitude within the block, given the binned mean-subtracted flux density measurements (f_i) and their uncertainties (δ_i). We evaluated each $P_{\rm block}$ at $\sigma = 0$ to 2 Jy using 0.001 Jy steps. This range and step size is wide enough to capture the most probable value in each block and to finely sample the function. By taking the most likely variability amplitude from each block, we can create a single cumulative distribution function (CDF) for each band. In order to illustrate the range of possible CDFs that are consistent with our data, we numerically sample the probability function for each block 100 times and create 100 additional CDFs. Figure 5 shows the region containing the central 68 CDFs created in this way for each wavelength.

Numerical simulations predict constant or increasing fractional variability with decreasing wavelength in the millimeter/submillimeter portion of the SED (e.g., Goldston et al. 2005; Dexter & Fragile 2013; Chan et al. 2015). While the allowed regions for the SPIRE CDFs of the variability amplitude overlap in Figure 5, the 0.25 and 0.5 mm regions are mostly distinct, and there is a clear trend of decreasing variability amplitude with wavelength, suggestive of a falling SED from 0.5 to 0.25 mm.

The distribution of 1.3 mm variability is notably different from the SPIRE curves in Figure 5. There is a long tail of high-amplitude variations not seen in the submillimeter light curves. This may be the result of catching Sgr A* during a quiet state, as past ground-based measurements of Sgr A* in the 0.45 and 0.35 mm atmospheric windows differed by several Jy (Dent et al. 1993; Serabyn et al. 1997; Pierce-Price et al. 2000; Marrone et al. 2006, 2008; Yusef-Zadeh et al. 2006). A quiet state is also suggested by the *XMM-Newton* light curves shown in Figures 2 and 3, which show no flare event with a 2–10 keV luminosity greater than 1.8×10^{34} erg s^{-1}. The absence of a larger flare in our X-ray light curves is consistent with the flare rate inferred from more than 800 hr of *Chandra* monitoring of Sgr A* (~1 day^{-1} above 10^{34} erg s^{-1}; Neilsen et al. 2013). The 1.3 mm light curve has a duration nearly three times that of the SPIRE light curve, and also extends over many years and therefore includes more of the long term fluctuations that can be expected from AGN variability.

4.2. 0.35–0.5 mm Color Changes

In Figure 6 we again plot the SPIRE light curves, but now show how the 0.5–0.35 mm flux density difference changes with time. In the first interval, we see a red color following our largest observed feature, from 05:00 to 08:00 UT. Notably, the flare falls off even faster at 0.25 mm than it does at 0.35 or 0.5 mm. The reddened color as flux density decreases is suggestive of a cooling process. The expanding-blob model for features in the submillimeter light curve of Sgr A* should exhibit a blue-first fall off in flux reminiscent of what we observe, yet the simultaneous rise at all wavelengths is not consistent with the most naive blob models. It is somewhat harder to predict how color changes should manifest in more complex occultation models where both absorption and adiabatic expansion take place simultaneously (Yusef-Zadeh et al. 2010).

During our second observing interval, the light curves exhibit a clear pattern of relatively red local maxima, and relatively blue local minima. This pattern indicates a larger absolute amplitude of variation for the longer-wavelength band. This pattern is less evident in the first interval, though there is some hint of a similar pattern in the smaller flares and the largest flare is brightest at 0.5 mm for most of its duration. This seeming change in the spectrum of the flaring emission between the first and second intervals may indicate that the quiescent 0.5–0.25 mm spectrum also changed, but without a way to directly measure the absolute flux density of Sgr A* we can only speculate.

4.3. Power Spectrum Analysis

We analyzed the power spectra of variations in the SPIRE Sgr A* light curves. To do this we combined the spectral averaging technique of Welch (1967)—to provide a high fidelity estimate of the power spectrum—and the Monte Carlo fitting approach of Uttley et al. (2002)—to properly account for the effects of our sampling pattern, aliasing, and red-noise leak on the shape of our power spectra.

Welch's method involves dividing a time series into overlapping segments, apodizing and Fourier transforming each, and then averaging the power at each frequency. We chose to use segment lengths 1/3 as long as our 12.75 hr observing intervals in order to closely match the timescale we used in our analysis in Section 4.1. We used 50% overlap as suggested by Press et al. (2002). After applying Welch's method to each of our two 12.75 hr intervals, we combined the results to produce one average power spectrum. Figure 7 shows the final power spectrum for our 0.5 mm light curve. For clarity we do not show the 0.35 mm or 0.25 mm power spectra. They

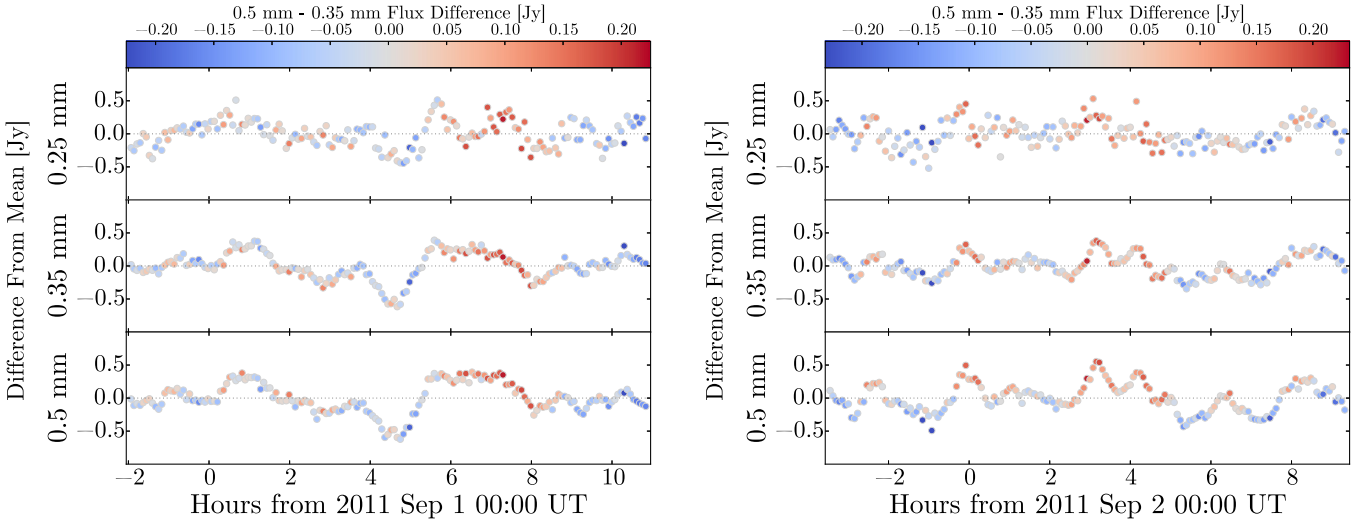

Figure 6. SPIRE light curves with flux density measurements color-coded to show the 0.5–0.35 mm flux density difference. The left panel shows the light curves from the first interval and the right panel shows the light curves from the second interval.

are similar though, as expected based on the shape of the light curves, but less well determined.

We modeled our light curve as arising from a power law noise process with $P(\nu) \propto \nu^{-\beta}$. To find the best-fitting power law slope, β, we followed Uttley et al. (2002) and simulated a large number of light curves with a given slope, sampled them according to the sampling pattern defined by our observations, computed their power spectra in the same way as for our Sgr A* light curves, and then used the distribution of simulated spectra to define a goodness of fit metric.

For a given β, we used the method of Timmer & Koenig (1995) to simulate light curves. To ensure we captured the effects of aliasing and red noise leak in our simulated spectra, we produced synthetic light curves that were 200 times as long, sampled 10 times as frequently as our observed light curves. These were then sampled at the same rate as our observations and divided into 100 pairs of 12.75 hr light curves. From each light curve, a best fit-slope was subtracted, as this was a necessary step in the reduction of our observed light curves (Section 2.1). Finally, a single power spectrum for each pair was computed using the same approach used for our observed light curves. This process is then repeated 100 times to yield 10^4 simulated spectra.

For each of the 10^4 simulated spectra, we computed the quantity

$$\chi^2_{\rm dist} = \sum_{\nu} \frac{[P_{{\rm sim},i}(\nu) - \overline{P_{\rm sim}}(\nu)]^2}{\sigma_{\rm sim}(\nu)^2}, \quad (5)$$

where $P_{{\rm sim},i}$ is a single simulated spectrum, $\overline{P_{\rm sim}}(\nu)$ is the mean of all the simulated spectra, and $\sigma_{\rm sim}(\nu)$ is the standard deviation of the spectra at each frequency (Uttley et al. 2002). We then computed a similar quantity for our observed power spectrum, $P_{\rm obs}(\nu)$,

$$\chi^2_{\rm dist,obs} = \sum_{\nu} \frac{[P_{\rm obs}(\nu) - \overline{P_{\rm sim}}(\nu)]^2}{\sigma_{\rm sim}(\nu)^2}, \quad (6)$$

scaling $\overline{P_{\rm sim}}(\nu)$ and $\sigma_{\rm sim}(\nu)$ by a common factor in order to minimize $\chi^2_{\rm dist,obs}$. Then we compared $\chi^2_{\rm dist,obs}$ to the distribution of $\chi^2_{\rm dist}$ defined by the 10^4 simulated spectra. The rejection probability for a given β is taken as the percent of the simulated light curves with $\chi^2_{\rm dist}$ smaller than $\chi^2_{\rm dist,obs}$. We plot one minus the rejection probability versus β in Figure 8. Our best-fit power law slope is $\beta = 2.40$ with a 95% confidence interval that spans from $\beta = 2.16$ to $\beta = 2.73$. We show our best fit model spectrum and associated errorbars in Figure 7. For comparison with our Monte Carlo-based approach, we also performed a basic fit of a line to our observed spectrum in log–log space. In this case we recover $\beta = 2.25$, which is less steep than we find following Uttley et al. (2002), yet still within the 68% confidence interval.

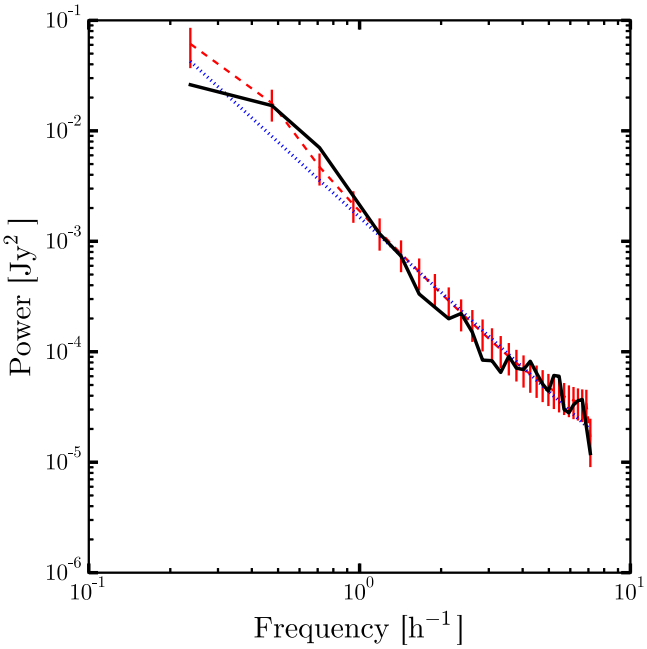

Figure 7. Observed (black curve) and fitted power spectra for our 0.5 mm Sgr A* light curve. The power spectra for the 0.25 and 0.35 mm light curves are similar, though less well determined. We used Welch's method to estimate the power spectrum as discussed in the text. The red dashed curve and error bars show the best fit spectrum, corresponding to $\beta = 2.4$, resulting from our Monte Carlo analysis based on Uttley et al. (2002). The blue dotted curve represents the best linear fit to the spectrum on log–log space, and suggests $\beta = 2.25$.

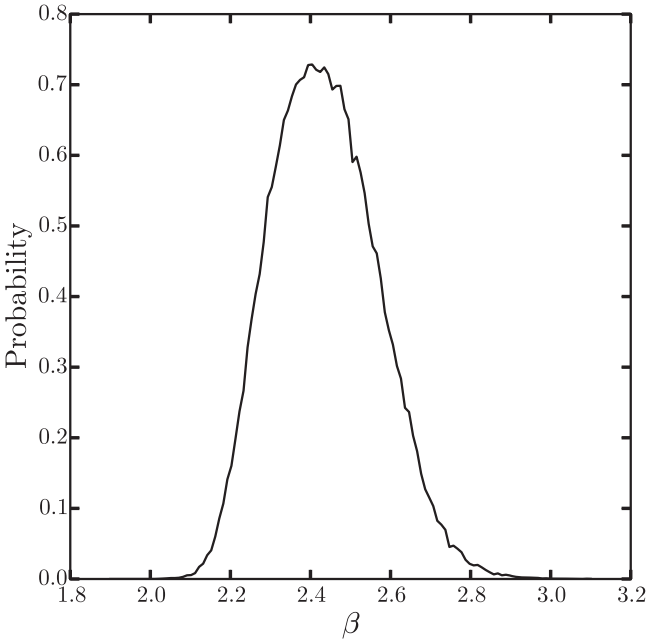

Figure 8. Results of our Monte Carlo fitting procedure for the power-law index of our observed power spectrum (based on Uttley et al. 2002).

Our derived spectral slope is very similar to the $\beta = 2.3^{+0.8}_{-0.6}$ measured at 1.3 mm by Dexter et al. (2014). Those authors also noted a break in the power spectrum at 8^{+3}_{-4} hr, which is a longer timescale than we have access to in our 12.75 hr intervals. Meyer et al. (2009) also found a slope of $\beta = 2.1 \pm 0.5$ at infrared wavelengths (mostly 2.2 μm), but with a spectral break around 2.5 hr, and Hora et al. (2014) found consistent characteristics at 4.5 μm. The consistency in slope from 1.3 mm, through the SPIRE bands, out to the IR is not unexpected, as emission at all of these wavelengths is expected to arise very close to the black hole, and therefore to be subject to the same variations in the accretion process.

5. CONCLUSIONS

In this work we have presented the longest continuous submillimeter observations of Sgr A*, using 25.5 hr of data from the SPIRE instrument aboard the *Herschel Space Observatory*. These data have provided a first lower bound on the SED of Sgr A* at 0.25 mm and characterized the wavelength and temporal spectra of its submillimeter variations. While *Herschel* is no longer operational, the Atacama Large Millimeter/Submillimeter Array (ALMA) can make ground-based measurements from 3 to 0.35 mm at high sensitivity, which can provide further constraints at similar wavelengths. In particular, the spatial resolution afforded by ALMA will be adequate to isolate Sgr A* from its surroundings, which was not possible with *Herschel*. Such data can more fully characterize the SED of this source and its fractional variability.

This work is based on observations made with Herschel, a European Space Agency Cornerstone Mission with significant participation by NASA. We thank Chi-Kwan Chan, Feryal Özel, and Dimitrios Psaltis for helpful discussions. DPM and JMS acknowledge support from NSF award AST-1207752 and from NASA through award OT1 cdowell 2 issued by JPL/Caltech. COH acknowledges support from an NSERC Discovery Grant and an Alexander von Humboldt Fellowship.

REFERENCES

An, T., Goss, W. M., Zhao, J.-H., et al. 2005, ApJL, 634, L49
Baganoff, F. K., Bautz, M. W., Brandt, W. N., et al. 2001, Natur, 413, 45
Baganoff, F. K., Maeda, Y., Morris, M., et al. 2003, ApJ, 591, 891
Bower, G. C., Markoff, S., Dexter, J., et al. 2015, ApJ, 802, 69
Brinkerink, C. D., Falcke, H., Law, C. J., et al. 2015, A&A, 576, A41
Chan, C.-k., Psaltis, D., Ozel, F., et al. 2015, ApJ, 812, 103
Chatfield, C. 1989, The Analysis of Timeseries, an Introduction (Oxford: Chapman and Hall Press)
de Bruyn, A. G. 1976, A&A, 52, 439
Dent, W. R. F., Matthews, H. E., Wade, R., & Duncan, W. D. 1993, ApJ, 410, 650
Dexter, J., Agol, E., Fragile, P. C., & McKinney, J. C. 2010, ApJ, 717, 1092
Dexter, J., & Fragile, P. C. 2013, MNRAS, 432, 2252
Dexter, J., Kelly, B., Bower, G. C., et al. 2014, MNRAS, 442, 2797
Dodds-Eden, K., Porquet, D., Trap, G., et al. 2009, ApJ, 698, 676
Dodds-Eden, K., Sharma, P., Quataert, E., et al. 2010, ApJ, 725, 450
Doeleman, S. S., Weintroub, J., Rogers, A. E. E., et al. 2008, Natur, 455, 78
Eckart, A., Baganoff, F. K., Morris, M., et al. 2004, A&A, 427, 1
Eckart, A., Baganoff, F. K., Morris, M. R., et al. 2009, A&A, 500, 935
Eckart, A., García-Marín, M., Vogel, S. N., et al. 2012, A&A, 537, A52
Eckart, A., Schödel, R., García-Marín, M., et al. 2008, A&A, 492, 337
Eckart, A., Schödel, R., Meyer, L., et al. 2006, A&A, 455, 1
Etxaluze, M., Smith, H. A., Tolls, V., Stark, A. A., & González-Alfonso, E. 2011, AJ, 142, 134
Falcke, H., Goss, W. M., Matsuo, H., et al. 1998, ApJ, 499, 731
Fish, V. L., Doeleman, S. S., Beaudoin, C., et al. 2011, ApJL, 727, L36
Genzel, R., Eisenhauer, F., & Gillessen, S. 2010, RvMP, 82, 3121
Genzel, R., Schödel, R., Ott, T., et al. 2003, Natur, 425, 934
Ghez, A. M., Salim, S., Weinberg, N. N., et al. 2008, ApJ, 689, 1044
Gillessen, S., Eisenhauer, F., Quataert, E., et al. 2006, ApJL, 640, L163
Gillessen, S., Eisenhauer, F., Trippe, S., et al. 2009, ApJ, 692, 1075
Goldston, J. E., Quataert, E., & Igumenshchev, I. V. 2005, ApJ, 621, 785
Griffin, M. J., Abergel, A., Abreu, A., et al. 2010, A&A, 518, L3
Haubois, X., Dodds-Eden, K., Weiss, A., et al. 2012, A&A, 540, A41
Hora, J. L., Witzel, G., Ashby, M. L. N., et al. 2014, ApJ, 793, 120
Hornstein, S. D., Matthews, K., Ghez, A. M., et al. 2007, ApJ, 667, 900
Kennea, J. A., Burrows, D. N., Kouveliotou, C., et al. 2013, ApJL, 770, L24
Marrone, D. P., Baganoff, F. K., Morris, M. R., et al. 2008, ApJ, 682, 373
Marrone, D. P., Moran, J. M., Zhao, J.-H., & Rao, R. 2006, JPhCS, 54, 354
Meyer, L., Do, T., Ghez, A., et al. 2009, ApJL, 694, L87
Neilsen, J., Nowak, M. A., Gammie, C., et al. 2013, ApJ, 774, 42
Pierce-Price, D., Richer, J. S., Greaves, J. S., et al. 2000, ApJL, 545, L121
Porquet, D., Predehl, P., Aschenbach, B., et al. 2003, A&A, 407, L17
Press, W. H., Teukolsky, S. A., Vetterling, W. T., & Flannery, B. P. 2002, Numerical Recipes in C++ : the Art of Scientific Computing
Read, A. M., Rosen, S. R., Saxton, R. D., & Ramirez, J. 2011, A&A, 534, A34
Sánchez-Portal, M., Marston, A., Altieri, B., et al. 2014, ExA, 37, 453
Serabyn, E., Carlstrom, J., Lay, O., et al. 1997, ApJL, 490, L77
Strüder, L., Briel, U., Dennerl, K., et al. 2001, A&A, 365, L18
Timmer, J., & Koenig, M. 1995, A&A, 300, 707
Turner, M. J. L., Abbey, A., Arnaud, M., et al. 2001, A&A, 365, L27
Uttley, P., McHardy, I. M., & Papadakis, I. E. 2002, MNRAS, 332, 231
Welch, P. D. 1967, IEEE Trans. Audio & Electroacoust., 15, 70
Yusef-Zadeh, F., Bushouse, H., Dowell, C. D., et al. 2006, ApJ, 644, 198
Yusef-Zadeh, F., Bushouse, H., Wardle, M., et al. 2009, ApJ, 706, 348
Yusef-Zadeh, F., Wardle, M., Bushouse, H., Dowell, C. D., & Roberts, D. A. 2010, ApJL, 724, L9
Yusef-Zadeh, F., Wardle, M., Heinke, C., et al. 2008, ApJ, 682, 361